Solar Energy Materials and Solar Cells 169 (2017) 8–12

Contents lists available at ScienceDirect

Solar Energy Materials and Solar Cells

journal homepage: www.elsevier.com/locate/solmat

Flexible perovskite solar cells with ultrathin Au anode and vapour-deposited perovskite film

Ming Xu[a], Jing Feng[a,*], Zhao-Jun Fan[a], Xia-Li Ou[a], Zhen-Yu Zhang[a], Hai-Yu Wang[a], Hong-Bo Sun[a,b]

[a] State Key Laboratory on Integrated Optoelectronics, College of Electronic Science and Engineering, Jilin University, 2699 Qianjin Street, Changchun 130012, People's Republic of China

[b] College of Physics, Jilin University, 119 Jiefang Road, Changchun 130023, People's Republic of China

ARTICLE INFO

Keywords:
Perovskite solar cells
Flexible
Vapour deposition
ITO-free

ABSTRACT

Flexible perovskite solar cells (pero-SCs) possessing high efficiency and low fabrication cost have been considered as the promising wearable energy supply devices in the near future. However, the intrinsic brittleness of the commonly used transparent conducting oxide electrodes is one of the limitations for the mechanical stability of flexible pero-SCs. Here we demonstrate the improved mechanical stability of flexible pero-SCs consisting of ultrathin Au electrode and vapour-deposited perovskite film. The thermal annealing-free perovskite film fabrication by vapour deposition is beneficial to the stability of the ultrathin Au electrode and contributes to the improved mechanical stability of the flexible pero-SCs. The power conversion efficiency for flexible pero-SCs maintains 74% of their initial efficiencies after 2000 bending cycles with a bending radius of 3.5 mm.

1. Introduction

Possessing the characteristics of both organic materials and inorganic materials, perovskite have far exceeded traditional semiconductor materials in many aspects, such as the relative smaller exciton binding energies, high absorption coefficient, long carrier diffusion lengths and ambipolar carrier transport [1]. The above mentioned characteristics have raised the prospect of perovskite materials as next generation photovoltaic materials and lots of studies for highly efficient perovskite solar cells (pero-SCs) have erupted recently [2,3]. Especially, the KRICT group has proposed the certified highest power conversion efficiency (PCE) of 22%, which is nearly comparable to the industrialized silicon solar cells [4]. Flexible pero-SCs have attracted considerable attention due to their excellent characteristics such as light weight, foldable and bendable, which contribute to their potential applications in wearable electronic with the advantages of convenient integration and versatile functionality [5,6]. However, the weak mechanical stability limits the practical application of the flexible pero-SCs. Cracks would emerge after bending due to the intrinsic brittleness of the commonly transparent conducting oxide electrode (ITO or FTO), which cause the rapid degradation and weak stability of the flexible pero-SCs [7]. Moreover, transparent conducting oxide materials are not up to the desirable ones for commercial flexible applications due to the high cost of indium and incompatibility of the high temperature processing with the flexible substrate [8,9].

Alternative conductive electrodes have been investigated in flexible pero-SCs such as carbon nanotubes, polymer conductor, titanium foil, silver nanowires and metallic films [10–13]. Among them, metallic films are one of the promising candidates as the electrode materials in flexible solar cells due to its excellent ductility and conductivity. The conductivity is related to the continuity of the metallic film, especially ultrathin film. The continuity of metallic film is governed by the nucleation and the growth kinetics on the substrates, which can be improved by seed layer and modification layer [14]. Ultrathin metallic films with high conductivity and transmittance can be obtained, which is desirable as transparent electrode for the optoelectronic devices. However, the ultrathin metallic film can hardly tolerate prolonged annealing treatment for the crystallization of perovskite film formed by solution process, which hinders the application of the ultrathin metallic film in the pero-SCs. Vapour deposition of the perovskite film is an ideal preparation technology for the ultrathin metallic electrode-based flexible pero-SCs by avoiding the annealing treatment. In this paper, we have demonstrated flexible pero-SCs using ultrathin Au electrode and vapour-deposited perovskite film. The flexible pero-SC by vapour deposition shows 9.05% of PCE. Meanwhile, the pero-SCs exhibit excellent flexibility and mechanical robustness. The efficiency of the flexible devices maintains 74% of their initial efficiencies after 2000 bending cycles with a radius of 3.5 mm.

* Corresponding author.
E-mail address: jingfeng@jlu.edu.cn (J. Feng).

http://dx.doi.org/10.1016/j.solmat.2017.04.039
Received 16 December 2016; Received in revised form 20 April 2017; Accepted 21 April 2017

2. Experimental details

2.1. Materials and chemicals

Patterned ITO substrates (10 Ω sq^{-1}) were supplied by CSG Holding Co., Ltd. PEDOT: PSS (Clevios P VP Al 4083) aqueous solutions and (6,6)-Phenyl C61 butyric acid methyl ester (PCBM) were purchased from Banhe Technology Co. Ltd. Methylammonium iodide (CH_3NH_3I, power, ≥99.5% purity) and lead chloride ($PbCl_2$, power, > 99.99% purity) were obtained from Xi'an Polymer Light Technology Corp. All the materials were used without further purification.

2.2. Fabrication of the ultrathin Au anode

Polished glass was cleaned sequentially in acetone, ethyl alcohol and deionized water by sonication for 30 min. After hydrophobic treating, the substrate was transferred into a glovebox filled with highly pure N_2. Then the photoresist (SU-8 2025, MicroChem Corp.) layer was spin-coated onto the substrate for 20 s at 5000 rpm and the thickness of SU-8 layer is about 150 nm. The substrate with the SU-8 layer was transferred into a thermal evaporation chamber. The MoO_3 seed layer was subsequent deposited on the SU-8 layer, which formed a composite layer. Finally, ultrathin Au film was deposited on the composite layer. The thickness of films was monitored by a quartz crystal oscillator and calibrated by Spectroscopic Ellipsometers (J. A. Woollam Co., Inc., USA). The surface morphology of Au films was taken on by atomic force microscope (AFM, Dimension Icon) and scanning electron microscope (SEM, JEOL JSM-7500F). The transmittance spectra of the samples were measured by a UV–vis spectrophotometer (UV-2550, Shimadzu Co., Inc., Japan).

2.3. Fabrication of perovskite film

Perovskite films were deposited by a dual-source evaporation system with quartz crucibles in the vacuum chamber. CH_3NH_3I and $PbCl_2$ were the organic and inorganic precursor salts, evaporated simultaneously from separate sources at 10^{-5} mbar with an as-deposited molar ratio of 4:1, based on the reading of the sensors above the crucibles [15]. The actual thickness of perovskite films was controlled by the third sensor beneath the substrates and calibrated by AFM and SEM. The crystallization of perovskite films was analyzed by X-ray diffraction, and the XRD patterns were collected on a Rigaku X-ray powder diffractometer using CuK < alpha > radiation (λ = 1.54050 Å).

2.4. Fabrication of characterization of perovskite solar cells

Referential ITO substrates were treated with UV − ozone for 15 min after cleaned. The ITO anode and ultrathin Au anode were then transferred into a glovebox filled with highly pure N_2. Hole transport layer with a thickness of ~60 nm was prepared by spin-coated PEDOT: PSS (Clevios P VP Al 4083) onto the anodes at 3500 rpm for 1 min and subsequently annealed at 95 ℃ for 30 min. Then the substrates with PEDOT: PSS were transferred to the dual-source evaporation system. After depositing perovskite layer (around 160 nm) in the vacuum chamber, PCBM electron transport layer with a thickness of ~ 45 nm was spin-coated a chlorobenzene solution of 20 mg ml^{-1} at 1000 rpm for 30 s. The cathode layer included 3 nm of Ca and 100 nm of Ag was thermally evaporated on the devices in a vacuum of 5×10^{-4}. The area of the devices was 4 mm^2. All the pero-SCs were tested in N_2 glovebox without encapsulated. To protecting flexible pero-SCs withstand bending test, a shape recoverable polymer (NOA63, Norland) was utilized as a supporting substrate [16]. The performance was measured using a Keithley 2400 source measure unit under a 1 sun simulated AM 1.5 G illumination. With an AAA class solar simulator (XES-70S1, san ei electric co.), the light intensity with 100 mW cm^{-2} was calibrated by standard Si photodiode detector equipped with a KG-5 filter. External quantum efficiencies were measured by an Enli Technology (Taiwan) EQE measurement system.

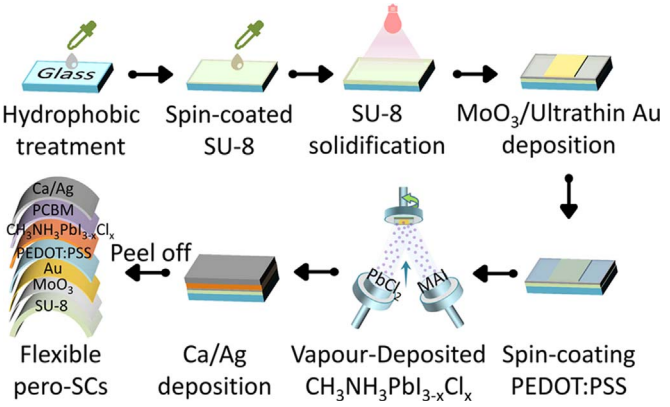

Fig. 1. Fabrication scheme of flexible pero-SCs with ultrathin Au anode and vapour-deposited perovskite film.

3. Results and discussion

The fabrication process of flexible pero-SCs with the ultrathin Au electrode (7 nm) is shown in Fig. 1. Composite layer (SU-8 modified layer and MoO_3 seed layer) beneath ultrathin Au film are used to suppress surface Au atoms diffuse and increase the electrical conductivity. The SU-8 layer would be peeled off from the hydrophobic glass substrate and thus the flexible planar pero-SCs with ultrathin Au electrode are obtained. The fabrication process of the vapour-deposited perovskite film has ruled out thermal annealing. PEDOT: PSS as the hole transport layer is prepared at 95 ℃ for 30 min for removing the solvent, which is the only heating procedure during the whole fabrication process of the pero-SCs.

As the transparent electrode of the pero-SCs, the continuity, conductivity and transmittance of metallic film are crucial factors for their application. The continuity of metallic film is governed by the nucleation and the growth kinetics on the substrates, which can be reacted to the surface morphology [17]. The surface morphology of 7 nm ultrathin Au film on various substrates have been investigated by scanning electron microscopy (SEM) and atomic force microscope (AFM) and shown in Fig. 2 and Supporting information Fig. S1. Au film deposited directly on the glass substrate shows large tortuous cracks and high roughness of 1.94 nm. This phenomenon can be explained by the Volmer-Weber growth mode of metallic film, higher bonding energy between Au atoms than that of the Au atom and glass substrate [18]. Unlike on the glass, Au film on SU-8 layer exhibits smaller cracks and low roughness of 0.997 nm. The significant improvement of surface morphology is attributed to the strong chemical covalent bonds between the SU-8 and Au atoms [19]. The MoO_3 seed layer could further improve nucleation sites and suppress surface diffusion of metal atoms [20]. Thus an ultra-smooth and continuous surface morphology is obtained by the SU-8/MoO_3/Au film. Simultaneously, the roughness has reached the minimum of 0.575 nm. The impact of the MoO_3 thickness on the surface morphology of the SU-8/MoO_3/Au film has also been investigated as shown in Supporting information Fig. S2.

Fig. 2d shows the resistance and transmittance of Au film with various substrates. The square resistance of 7 nm Au film deposited on glass, SU-8 layer and SU-8/MoO_3 layer is 401 Ω/□, 91 Ω/□ and 19 Ω/□, respectively. Ultrathin Au film deposited on SU-8/MoO_3 layer has the smallest resistance, which is attributed to the role of seed layer (MoO_3). Low resistance confirms the improvement of the continuity of Au film. Meanwhile, obvious difference in the transmittance can be observed from the photograph of the ultrathin Au films deposited on

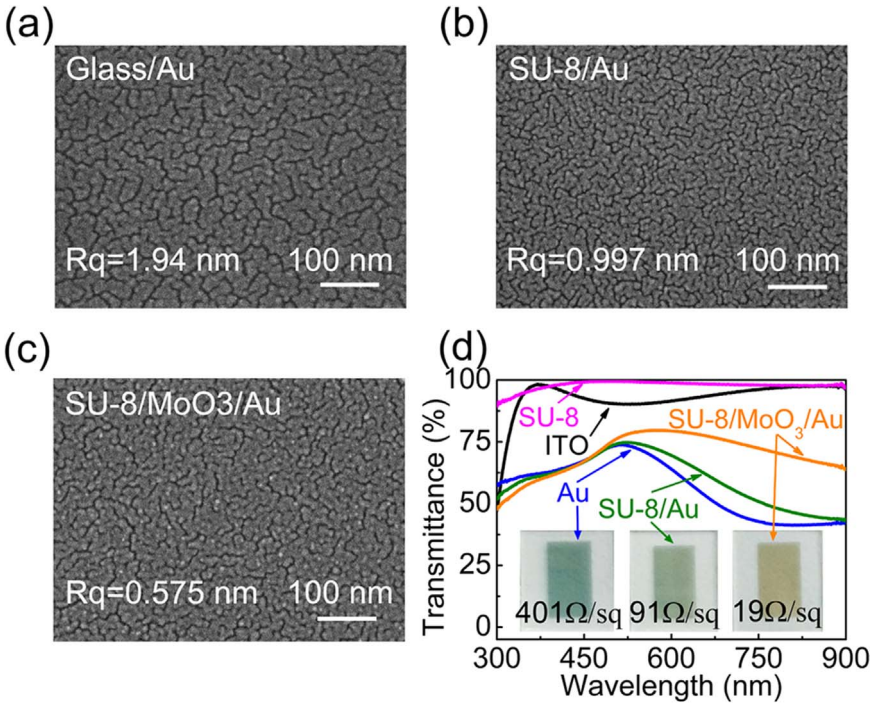

Fig. 2. Surface morphology and transmittance of ultrathin Au deposited on various substrates. (a-c) SEM images of 7 nm ultrathin Au deposited on glass (Glass/Au), SU-8 layer (SU-8/Au) and composite layer (SU-8/MoO_3/Au). (d) Transmittance spectra of referential ITO film, SU-8 film and ultrathin Au on various substrates: Inset shows the square resistance and photograph of Glass/Au, SU-8/Au and SU-8/MoO_3/Au.

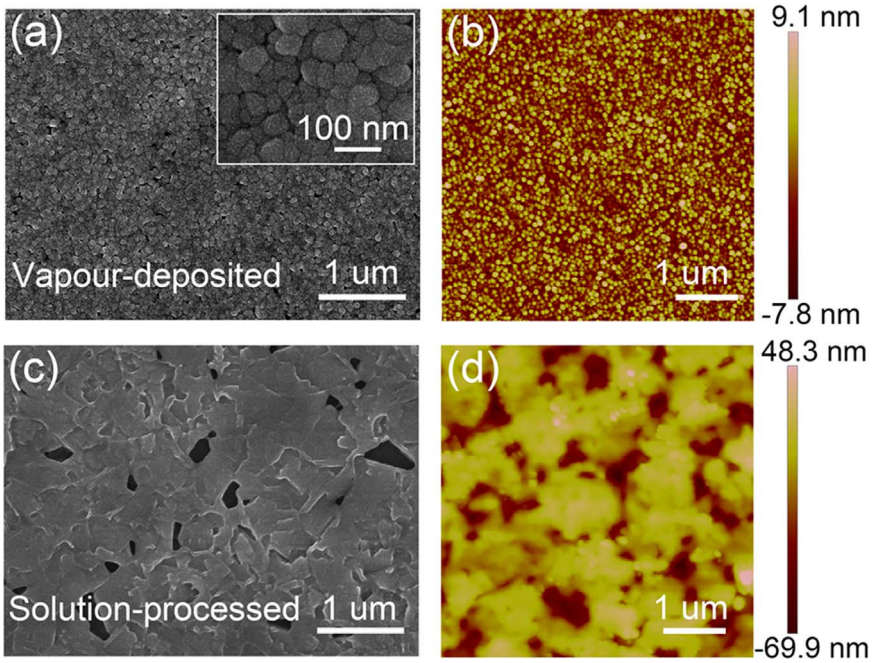

Fig. 3. SEM image (a) and AFM image (b) of vapour-deposited perovskite film. SEM image (c) and AFM image (d) of solution-processed perovskite film. The high magnification SEM image of vapour-deposited perovskite film (inset).

various substrates (the inset of Fig. 2d). Significantly improved transmittance is observed from the Au film deposited on SU-8/MoO_3 layer from 500 nm to 900 nm, which would be beneficial to the high efficiency of the solar cells. The SU-8 layer beneath Au film has a positively effect on the transparency, which can be attributed to extinct surface plasmon resonances [21,22] and refractive index-matching affect [23]. With the increasing thickness of the MoO_3 seed layer, the weakened surface resonance absorption and good transmittance indicates Au films becomes more smooth and continuous (see Supporting information Fig. S3). However, when the thickness of MoO_3 layer increased to 5 nm, a lot of cracks appear after spin-coating PEDOT: PSS solution onto the SU-8/MoO_3/Au film (Fig. S3b). Thus 3 nm MoO_3 was employed as the seed layer for the follow preparation of the pero-SCs.

Compared to the surface morphology of the solution-processed perovskite film from SEM and AFM images, the vapour-deposited perovskite film without the thermal annealing has uniform, pinhole-free and continuous surface as can be seen in Fig. 3. The crystal size of the vapour-deposited film is relative smaller (60–70 nm in diameter)

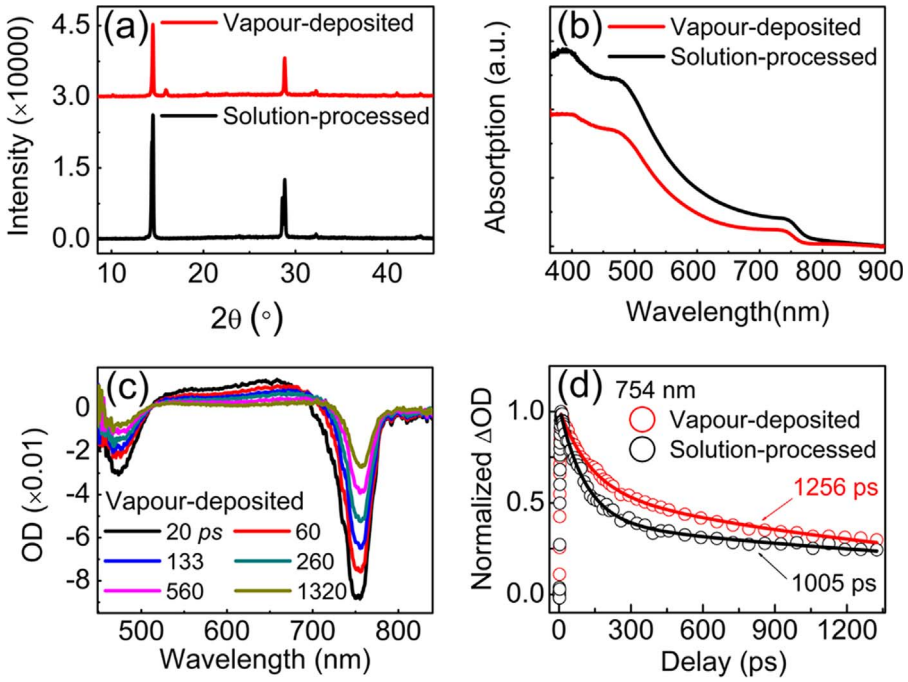

Fig. 4. Characteristics of perovskite film fabricated by vapour deposition and solution process. (a) XRD spectra. (b) UV–vis absorbance spectra. (c) Time-resolved pump-probe measurement for vapour-deposited perovskite film at 754 nm. (d) The decay kinetics examine of the related band edge bleaching at the bandgap. The thickness of vapour-deposited and solution-processed perovskite film is 160 nm and 300 nm, respectively.

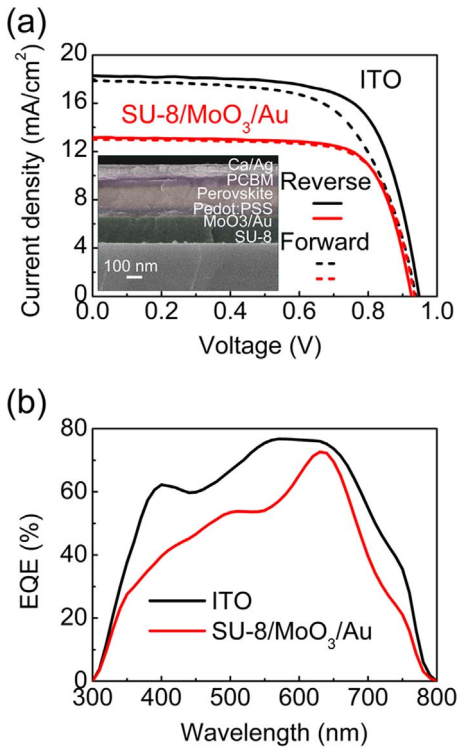

Fig. 5. (a) J–V curves in reverse and forward scan for the pero-SCs based on both ITO and ultrathin Au anode: Inset shows SEM cross-sectional image of the device based on ultrathin Au anode. (b) EQE spectra of pero-SCs based on both ITO and ultrathin Au anode.

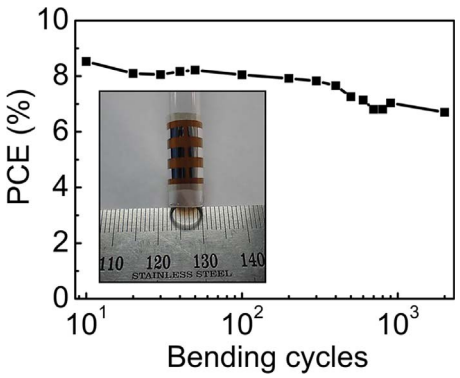

Fig. 6. PCEs of flexible pero-SCs based on ultrathin Au anode as a function of bending cycles at a radius of 3.5 mm: Inset shows photograph of corresponding flexible pero-SCs.

than that of the solution-processed film (200–400 nm in diameter), and the pinhole is obviously fewer. Meanwhile, the roughness of the vapour-deposited perovskite film is 2.55 nm, which is one order of magnitude lower than that of the solution-processed film (18.2 nm). The much decreased pinholes and surface roughness are important factors for the high efficiency of the pero-SCs.

The crystal qualities of perovskite films fabricated by solution process and vapour deposition are analyzed with XRD, steady and transient absorption (TA) spectra (Fig. 4). As shown in Fig. 4a, vapour-deposited perovskite film exhibits identical peak positions with that of solution-processed film, assigned to the 110, 220 and 330 diffraction peaks at 14.4°, 28.5°and 43.5°, respectively. The consistent peaks indicate that both vapour-deposited and solution-processed films have produced the same mixed-halide perovskite orthorhombic lattices [24]. Moreover, the steady absorption spectra of both perovskite films have the same line-shape (Fig. 4b). The performance of the pero-SCs is sensitive to the film morphology and deeper understanding comes from the femtosecond transient dynamics measurements. The TA spectra of both films given in Fig. 4c (pumped under 400 nm with intensity at 15.4 μJ cm^{-2}) show two ground bleaching signals as well as the broad excited-state absorption centered at 600 nm. The peak at 754 nm (~1.644 eV) is approximately equal to the band gap energy and the peak at 475 nm (2.611 eV) is previously considered as the transitions from VB2 to CB1 in the dual valence band structure [25]. We mainly focus on the characteristic of the 754 nm photoinduced bleach in order to probe the band-edge charge carrier dynamics in film. These dynamics all shows the recovery of the photoinduced bleaching as free charge

carriers recombination, for the relaxation of the band-edge transition could last for a timescale of nanoseconds. Fig. 4d displays the carrier recombination dynamics of both perovskite films under the identical pump intensity. The kinetic decay rates of band-edge at ~ 754 nm become slower in the vapour-deposited perovskite films. Due to the morphology of solution-processed films provided the better environment for defects [26,27], the decay dynamics of solution-processed films shows faster recombination rate compared with that of vapour-deposited film. The lifetime of the solution-processed perovskite film is 1005 ps, while it increases to 1256 ps for vapour-deposited film. The increased lifetime for vapour-deposited film can be attributed to the fewer defect and would much benefit to the performance of the pero-SCs.

The current (J) – voltage (V) curves and external quantum efficiency (EQE) curves of the vapour-deposited flexible pero-SCs with ultrathin Au anode are summarized in Fig. 5. The vapour-deposited pero-SCs with ultrathin Au anode on the rigid substrates are shown in Supporting information Fig. S4. The pero-SCs with ITO anode are investigated for comparison. The cross-sectional SEM image of the pero-SCs with Au anode is shown in the inset of Fig. 5a. The flexible pero-SC fabricated on Au anode shows the short-circuit current density (Jsc) of 13.17 mA cm^{-2}, open-circuit voltage (Voc) of 0.93 V, fill factor (FF) of 73.89%, and PCE of 9.05%. The photovoltaic performances are not as high as that of the referential device, which has a Jsc of 18.28 mA cm^{-2}, a Voc of 0.95 V, an FF of 70.18%, and a PCE of 12.13%. The Jsc of the pero-SCs with ultrathin Au anode being lower than that of the pero-SC with ITO anode is mainly derived from the low transmittance of ultrathin Au from 350 nm to 600 nm (Fig. 2d), which is corresponding to EQE characteristics as shown in Fig. 5b. Notably, high FF can be observed from the device with ultrathin Au anode that owes to the ideal ohmic contact at the Au/PEDOT: PSS interface (ITO~4.8 eV, Au~5.1 eV and PEDOT: PSS~5.2 eV). Moreover, vapour-deposited perovskite film has high hysteresis index due to the small crystal size of perovskite film (60–70 nm in diameter) [28,29], and the small J-V hysteresis behaviours of both devices are given in Supporting information Table S1.

To investigate the mechanical stability, flexible pero-SCs with ultrathin Au anode and vapour-deposited perovskite film were bent over a roll with a curvature radius of 3.5 mm (Fig. 6). The performance was evaluated up to 2000 bending cycles and the device maintained 74% of its initial photovoltaic performance after bending. The Jsc and FF decrease from 13.17 mA cm^{-2}, 73.89% to 10.62 mA cm^{-2}, 61.85%, respectively, which lead to a small decay in the PCE of 26%. The detailed parameters of flexible cells under bending tests are completely exhibited in Supporting information Fig. S5. The flexible pero-SCs by vapour deposition using ultrathin Au as anode have been revealed to possess excellent mechanical stability.

4. Conclusions

Flexible pero-SCs fabricated by vapour deposition have been successfully constructed on ultrathin Au anode. Ultra-smooth surface and excellent conductivity of ultrathin Au film has been realized by integrating the SU-8 modified layer and MoO_3 seed layer. Meanwhile, vapour-deposited perovskite film is beneficial to the stability for ultrathin Au anode based flexible pero-SCs. A PCE of 9.05% has been realized by the flexible pero-SCs with ultrathin Au anode and vapour-deposited perovskite film. The flexible pero-SCs could maintain 74% of initial PCE after 2000 bending cycles with a radius of 3.5 mm. This study promotes the development of flexible pero-SCs and be expected to aid in realization of wearable energy power applications.

Acknowledgements

The authors gratefully acknowledge support from the 973 Project (2013CBA01700) and NSFC (Grant Nos. 61675085, 61322402, 61590930, 51373064 and 61505065).

Appendix A. Supplementary material

Supplementary data associated with this article can be found in the online version at http://dx.doi.org/10.1016/j.solmat.2017.04.039.

References

[1] M.A. Green, A.H. Baillie, H.J. Snaith, The emergence of perovskite solar cells, Nat. Photon. 8 (2014) 506–514.
[2] X. Li, D.Q. Bi, C.Y. Yi, J.D. Décoppet, J.S. Luo, S.M. Zakeeruddin, A. Hagfeldt, M. Grätzel, A vacuum flash–assisted solution process for high-efficiency large-area perovskite solar cells, Science 353 (2016) 58–62.
[3] W.S. Yang, J.H. Noh, N.J. Jeon, Y.C. Kim, S. Ryu, J. Seo, S. Il Seok, High-performance photovoltaic perovskite layers fabricated through intramolecular exchange, Science 348 (2015) 1234–1237.
[4] NERL Efficiency chart. ⟨http://www.nrel.gov/ncpv/images/efficiency_chart.jpg⟩.
[5] H.F. Lu, J.S. Sun, H. Zhang, S.M. Lu, W.C.H. Choy, Room-temperature solution-processed and metal oxide-free nano-composite for the flexible transparent bottom electrode of perovskite solar cells, Nanoscale 8 (2016) 5946–5953.
[6] B. Susrutha, L. Giribabua, S.P. Singh, Recent advances in flexible perovskite solar cells, Chem. Commun. 51 (2015) 14696–14707.
[7] K. Poorkazem, D.Y. Liu, T.L. Kelly, Fatigue resistance of a flexible, efficient, and metal oxide-free perovskite solar cell, J. Mater. Chem. A 3 (2015) 9241–9248.
[8] S.S. Shin, W.S. Yang, J.H. Noh, J.H. Suk, N.J. Jeon, J.H. Park, J.S. Kim, W.M. Seong, S. Il Seok, High-performance flexible perovskite solar cells exploiting Zn2SnO4 prepared in solution below 100°C, Nat. Commun. 6 (2015) 7410.
[9] X.B. Xu, Q. Chen, Z.R. Hong, H.P. Zhou, Z.H. Liu, W.H. Chang, P.Y. Sun, H.J. Chen, N.D. Marco, M.K. Wang, Y. Yang, Working mechanism for flexible perovskite solar cells with simplified architecture, Nano Lett. 15 (2015) 6514–6520.
[10] Il Jeon, T. Chiba, C. Delacou, Y.L. Guo, A. Kaskela, O. Reynaud, E.I. Kauppinen, S. Maruyama, Y. Matsuo, Single-walled carbon nanotube film as electrode in indium-free planar heterojunction perovskite solar cells: investigation of electron-blocking layers and dopants, Nano Lett. 15 (2015) 6665–6671.
[11] K. Sun, P.C. Li, Y.J. Xia, J.J. Chang, J.Y. Ouyang, Transparent conductive oxide-free perovskite solar cells with PEDOT: pss as transparent electrode, ACS Appl. Mater. Interfaces 7 (2015) 15314–15320.
[12] M. Lee, Y. Jo, D.S. Kimb, Y.S. Jun, Flexible organo-metal halide perovskite solar cells on a Ti metal substrate, J. Mater. Chem. A 3 (2015) 4129–4133.
[13] A. Kim, H. Lee, H.C. Kwon, H.S. Jung, N.G. Park, S. Jeong, J. Moon, Fully solution-processed transparent electrodes based on silver nanowire composites for perovskite solar cells, Nanoscale 8 (2016) 6308–6316.
[14] R.A. Hatton, M.R. Willis, M., A. Chestersa, D. Briggs, A robust ultrathin, transparent gold electrode tailored for hole injection into organic light-emitting diodes, J. Mater. Chem. 13 (2003) 722–726.
[15] O. Malinkiewicz, C.R. Carmona, A. Soriano, E. Bandiello, L. Camacho, M.K. Nazeeruddin, H.J. Bolink, Metal-oxide-free methylammonium lead iodide perovskite-based solar cells: the influence of organic charge transport layers, Adv. Energy Mater. 4 (2014) 1400345.
[16] M. Park, H.J. Kim, I. Jeong, J. Lee, H. Lee, H.J. Son, D.E. Kim, M.J. Ko, Mechanically recoverable and highly efficient perovskite solar cells: investigation of intrinsic flexibility of organic–inorganic perovskite, Adv. Energy Mater. 5 (2015) 1501406.
[17] E.D. Gaspera, Y. Peng, Q.C. Hou, L. Spiccia, U. Bach, J.J. Jasieniak, Y.B. Cheng, Ultra-thin high efficiency semitransparent perovskite solar cells, Nano Energy 13 (2015) 249–257.
[18] N. Kaiser, Review of the fundamentals of thin-film growth, Appl. Opt. 41 (2002) 3053.
[19] Y.G. Bi, J. Feng, J.H. Ji, Y. Chen, Y.S. Liu, Y.F. Li, Y.F. Liu, X.L. Zhang, H.B. Sun, Ultrathin and ultrasmooth Au films as transparent electrodes in ITO-free organic light-emitting devices, Nanoscale 8 (2016) 10010–10015.
[20] S. Schubert, M. Hermenau, J. Meiss, L.M. Meskamp, K. Leo, Oxide sandwiched metal thin-film electrodes for long-term stable organic solar cells, Adv. Funct. Mater. 22 (2012) 4993–4999.
[21] J.R. Heath, Size & ependent surface-plasmon resonances of bare silver particles, Phys. Rev. B. 40 (1989) (9985-9982).
[22] S.K. Kim, H.S. Ee, W. Choi, S.H. Kwon, J.H. Kang, Y.H. Kim, H. Kwon, H.G. Park, Surface-plasmon-induced light absorption on a rough silver surface, Appl. Phys. Lett. 98 (2011) 011109.
[23] Y.F. Liu, J. Feng, Y.F. Zhang, H.F. Cui, D. Yin, Y.G. Bi, J.F. Song, Q.D. Chen, H.B. Sun, Improved efficiency of indium-tin-oxide-free flexible organic light-emitting devices, Org. Electron. 15 (2014) 2661–2666.
[24] M.Z. Liu, M.B. Johnston, H.J. Snaith, Efficient planar heterojunction perovskite solar cells by vapour deposition, Nature 501 (2013) (395-395).
[25] J.S. Manser, P.V. Kamat, Band filling with free charge carriers in organometal halide perovskites, Nat. Photon. 8 (2014) 737–743.
[26] D.W. deQuilettes, S.M. Vorpahl, S.D. Stranks, H. Nagaoka, G.E. Eperon, M.E. Ziffer, H.J. Snaith, D.S. Ginger, Impact of microstructure on local carrier lifetime in perovskite solar cells, Science 348 (2015) 683–686.
[27] S. Draguta, S. Thakur, Y.V. Morozov, Y.X. Wang, J.S. Manser, P.V. Kamat, M. Kuno, Spatially non-uniform trap state densities in solution-processed hybrid perovskite thin films, J. Phys. Chem. Lett. 7 (2016) 715–721.
[28] H.S. Kim, N.G. Park, Parameters affecting I – V hysteresis of CH3NH3PbI3 perovskite solar cells: effects of perovskite crystal size and mesoporous TiO2 layer, J. Phys. Chem. Lett. 5 (2014) 2927–2934.
[29] N.J. Jeon, J.H. Noh, Y.C. Kim, W.S. Yang, S. Ryu, S. Il Seok, Solvent engineering for high-performance inorganic–organic hybrid perovskite solar cell, Nat. Mater. 13 (2014) 897–903.